PHYSICAL REVIEW B **102**, 184116 (2020)

Manipulation of giant negative Poisson's ratios in three-dimensional graphene networks

Shukuan Guo and Hong Sun*
School of Physics and Astronomy, and Key Laboratory of Artificial Structures and Quantum Control (Ministry of Education), Shanghai Jiao Tong University, Shanghai 200240, China

(Received 15 September 2020; revised 9 November 2020; accepted 12 November 2020; published 30 November 2020)

Three-dimensional (3D) graphene networks (3DGNs) have drawn broad interest recently for their superior physical properties, such as large surface area, high strength, superelasticity, tunable band gaps and topological properties, with potential applications in high-capacity energy storage and novel electronic systems. In this work, giant negative Poisson ratios (NPRs) up to −8.5 and colossal auxetic transverse contraction (or expansion) of more than 40% (or 20%) in 3DGNs are predicted by first-principles calculations, adding another extraordinary mechanical property to 3DGNs. A mechanism dominated by sp^3-carbon bond angle distortion and in-plane anisotropy variation is revealed that can explain such exceptional NPRs in 3DGNs. Furthermore, easy manipulation and enhancement of NPRs are achieved by applying biaxial stresses which increase the in-plane anisotropy of 3DGNs, providing a way for the rational design and application of NPR materials. These discoveries will deepen our understandings of 3DGNs and broaden their technological applications as multifunctional materials.

DOI: 10.1103/PhysRevB.102.184116

I. INTRODUCTION

Materials with counterintuitive physical properties, such as negative Poisson ratios (NPRs) [1], negative compressibility [2], and negative thermal expansion [3], have attracted considerable attention for years from both fundamental science and practical application points of view. Poisson's ratio (PR), expressed as $\nu = -\epsilon_T/\epsilon_L$, is the negative ratio of the induced transverse strain ϵ_T to the applied longitudinal strain ϵ_L and is predicted to vary between −1 and 0.5 for isotropic materials [1]. NPR materials, also known as auxetic materials, show abnormal mechanical properties under structural deformations, not easily obtainable in conventional materials. They display synclastic curvature, enhanced shear and indentation resistance, and increased fracture toughness [4], which enable them to have widespread technological applications in various fields, such as aerospace [5], sensitive detectors [6], surgical implants, biomedicine [7], sport protective equipment, and crash energy absorption parts [4,8].

Quite a few materials have been found to exhibit NPR effects based on the elastic theory and the experimentally measured or theoretically calculated elastic constants C_{ij} [5,9], and some have been studied for their underlying mechanisms to broaden the exploration. For example, hierarchical structure is the common and unique building block in many natural and organic auxetic biomaterials [10]. The re-entrant geometries play a decisive role in the auxetic behavior of polymer foams [4]. The NPR in simple cubic metals can be explained by an octahedral mode [5]. The buckling structures, either intrinsically existed or induced by defects, can lead to NPRs in two-dimensional (2D) materials [11–13]. In layered materials like black phosphorous, the dispersive van der Waals interaction can result in the auxetic property [14]. The surface effect is a main origin of the auxeticity in nanoplates and nanowires [15,16]. And the tetrahedral rotation and dilation is invoked to explain the auxetic property in α cristobalite [17]. Very recently, NPR materials based on rotating polygons in both macroscopic and molecular scales have drawn renewed research interests [18–20]. However, known NPR materials with strong auxetic effects (NPR < -1) are still very limited and exist only in anisotropic materials [9,21,22], which hinders optimal choices in their applications, and easy-tunable auxetic materials driven by underlying mechanisms await to be discovered. Furthermore, materials with strong auxetic behavior and high strengths originated from (inorganic) atomic or molecular structures are important, especially for applications in nanoscience.

Molecular networks with NPRs can be designed at the molecular level, and hypothetical all-carbon sp^2 bonding three-dimensional (3D) crystalline networks were predicted to show unusual mechanical and thermal properties with minor NPR (−0.2) as early as 1993 [23]. Recently, various 3D graphene networks (3DGNs), comprising cross-linked graphene sheets with sp^2 or mixed sp^2-sp^3 hybridization, have both been synthesized experimentally [24–30] and identified theoretically [31–35], which demonstrates excellent physical and chemical properties superior to 2D graphene. The unique combination of low mass density, large surface area, high strength [30], superelasticity [28], negative linear compressibility [31], tunable band gaps, and novel topological properties [31,35,36], renders 3DGNs excellent materials for various technological applications, such as high-capacity energy storage [24,29,31,33], novel topological electronic devices [31,35,36], and broadband micro- and terahertz-wave absorptions [25,27], to mention a few. Most previous reports focused on the mechanical, optoelectronic, electrochemical, and topological properties of various 3DGNs, a very few

---

*hsun@sjtu.edu.cn

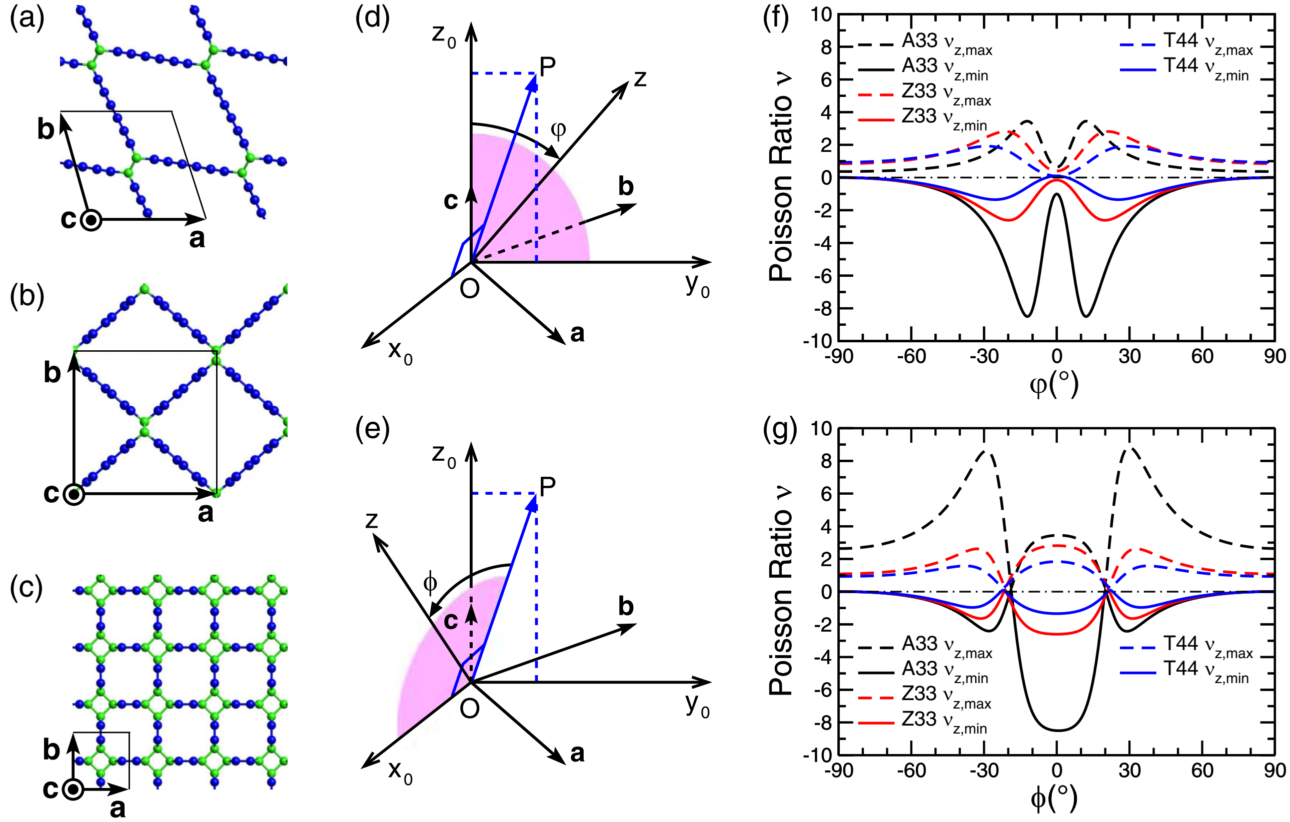

FIG. 1. (a)–(c) The crystal structures (top views) of A33, Z33, and T44 3DGN allotropes, with their 3D structural views and atomic positions given in Fig. S1 and Table S1 [see Supplemental Material (SM) [41]]. Hereinafter, the blue spheres represent carbon atoms with sp^2 bonding in the graphene nanoribbons and the green ones represent carbon atoms with sp^3 bonding at the link junctions. (d), (e) Relations of the strain direction Oz, the lattice vectors **a**, **b**, **c**, and the $\boldsymbol{P}$ direction strained along which gives the minimum PR ($\nu_{\min}$). The reference Cartesian coordinate (x_0, y_0, z_0) is established with the x_0 axis perpendicular to the cOP plane and the z_0 axis parallel to the vector **c**. (f), (g) The maximum (dashed line, $\nu_{z,\max}$) and minimum (solid line, $\nu_{z,\min}$) values of PR at different angles φ and ϕ when the longitudinal strain direction Oz rotates within the y_0Oz_0 and x_0OP planes, respectively, for A33 (black curves), Z33 (red curves), and T44 (blue curves).

of which have been studied to show either near-zero PR ($\approx$0.0025) under compressive strains up to 80% [28] or moderate NPRs (≈ -0.5) under large strains [26,37,38]. The structures of various 3DGNs can be divided into carbon random networks (CRNs) and crystalline networks, with the latter being further classified into carbon Kagome lattices (CKLs), interpenetrated graphene networks (IGNs), carbon honeycombs (CHCs), etc. as described in a recent review [35]. Experimentally, CRNs have been acquired by solvothermal self-assembly of graphene oxide [25–28], CHCs have been obtained by deposition of sublimated graphite [29], and IGN structures have been identified in cold compression of glassy carbon [30]. It is highly desirable to carry out more detailed experimental studies to synthesize high quality 3DGN samples and characterize their precise atomic structures. The auxetic behavior of CRNs and CHCs were studied previously which exhibit either near-zero PR ($\approx$0.0025) [28] or moderate NPRs (≈ -0.5) [26,37,38], and our calculations reveal that under different compressive strains CKLs tend to transform to IGNs with lower total energies after structure relaxation. So in the present paper, we focus on in-depth studies of the auxetic behavior of IGN-type 3DGNs proposed previously [31,39,40] using first-principles calculations, which show surprisingly giant NPRs up to -8.5 and their easy manipulations by biaxial stresses with an underlying NPR mechanism, adding another extraordinary mechanical property to 3DGNs as multifunctional materials.

II. COMPUTATIONAL DETAILS

A. Structures

We investigate three 3DGNs, assigned as A33, Z33, and T44, composed of armchair or zigzag sp^2 graphene nanoribbons jointly linked by sp^3 hybridized carbon atoms [31,39,40], as shown in Figs. 1(a)–1(c), which belong to monoclinic, orthogonal, and tetragonal crystal systems, respectively, with the calculated lattice constants given in Table I. Previous calculations show that Z33 has the lowest total energy among all identified 3DGNs [31,33,34,39,40]. These structures are energetically metastable with respect to graphite and have been verified as dynamically stable (without imaginary phonon frequency) by previous calculations [40] and our phonon calculations (see below). All of the calculated elastic constants C_{ij} listed in Table I satisfy the Born elastic stability condition [42]; that is, all eigenvalues of the elastic matrix are positive, indicating that these 3DGNs are also mechanically stable.

TABLE I. The calculated unit-cell lattice constants and elastic constants C_{ij} (in GPa) of the 3DGNs, where the elastic constants C_{ij} are projected in the Cartesian coordinate system (x_0, y_0, z_0), as discussed in Computational details and shown in Figs. 1(d) and 1(e).

	a (Å)	**b** (Å)	**c** (Å)	$\alpha(^\circ)$	$\beta(^\circ)$	$\gamma(^\circ)$
A33	9.663	9.696	4.322	90	90	108.73
Z33	12.148	12.147	2.465	90	90	90
T44	5.221	5.221	2.506	90	90	90

C_{ij}	C_{11}	C_{22}	C_{33}	C_{12}	C_{13}	C_{23}	C_{44}	C_{55}	C_{66}	C_{16}	C_{26}	C_{36}	C_{45}
A33	62	345	588	136	33	92	198	76	47	32	39	7	27
Z33	216	167	702	182	57	46	143	170	143				
T44	335	335	907	313	60	60	227	227	240				

B. First-principles calculations

First-principles calculations based on density-functional theory are performed by using the Vienna *ab initio* simulation package (VASP) [43]. The projector augmented wave (PAW) method is adopted to describe the electron-ion interactions [44]. The exchange-correlation energies of electrons are treated by the generalized gradient approximation (GGA) parametrized by Perdew, Burke, and Ernzerhof (PBE) [45]. The cutoff energy of the plane-wave basis is set at 600 eV, and the convergence criteria for the electronic and ionic relaxations are 10^{-7} eV and 5×10^{-7} eV, respectively. Monkhorst-Pack [46] k-point grids of $5 \times 5 \times 11$, $4 \times 4 \times 10$, and $9 \times 9 \times 9$ are adopted for the periodical unit cell of A33 and periodical $1 \times 1 \times 2$ supercell of Z33 and T44, respectively, to ensure the energy, stress, and force convergence reaching 1 meV per atom, 0.1 GPa, and 0.001 eV/Å. The supercell is used for Z33 and T44 because of their short **c** axes (see Table I) so that all the 3DGNs have about the same layers of atoms along their **c** axes when tensile or compression deformations are introduced. The uniaxial or biaxial tensile loading process is simulated by a quasistatic displacement-controlled deformation process, similar to that in our previous work on indentation strength [47,48], in which the lattice vectors of the unit or supercell of the 3DGNs are incrementally deformed, say, in the z direction, by applying tensile strains with an incremental strain step of $\Delta\epsilon_{zz} = 0.005$. At each step, the applied tensile (true) strain ϵ_{zz} is fixed to determine the calculated tensile stress σ_{zz}, while the other five independent components of the strain tensors and all the atoms inside the unit or supercell are simultaneously relaxed until the following conditions are met: (i) the biaxial stress perpendicular to the applied strain direction, say σ_{yy}, reaches a fixed value, $\sigma_{yy} = \sigma_{yy}^{(0)}$, which is set to zero in the uniaxial loading process, (ii) all the other four components (except σ_{zz}) of the Hellmann-Feynman stress tensor are negligibly small (<0.1 GPa), and (iii) the force on each atom becomes practically zero (<0.001 eV/Å). The shape of the (deformed) unit or supercell, the positions of the atoms, the induced transverse strain variation $\Delta\epsilon_T$ (or the variation of the cross section area ΔS) vertical to the applied strain $\Delta\epsilon_{zz}$, and the relation between the tensile stress σ_{zz} and the corresponding strain ϵ_{zz} are determined completely at each step by this constrained atomic relaxation, including the effect of the biaxial stress $\sigma_{yy}^{(0)}$. Two useful kinds of total strains, the true strain ϵ_T and engineering strain ϵ_E [49], can be defined, which are related to each other by $\epsilon_T = \Sigma\Delta\epsilon_T^{(i)} = \int_{l_0}^{l} dl_T/l_T = \ln(l/l_0) = \ln(\epsilon_E + 1)$ with $\epsilon_E = (l - l_0)/l_0$. The definition of the true total strain is used in all our reported results. As demonstrated in the previous calculations on 3DGNs [50–52], the dispersive van der Waals interaction is treated by the DFT-D2 method [53] in all our calculations. To examine the dynamical stability of the equilibrium and the deformed 3DGN structures, their phonon spectra are calculated by using the PHONOPY code based on the finite-displacement method [54].

C. Direction-dependent Poisson ratio calculations

PR is an orientation-dependent property in anisotropic crystals, which can be determined by $\nu_{ij} = -s_{ij}/s_{ii}$, where s_{ij} and s_{ii} are the elastic compliance coefficients obtained from the calculated elastic constants C_{ij} (see Table I) of the 3DGNs, and $i, j = x, y, z$ indicate the axis directions of a chosen Cartesian coordinate system (CCS), with i the direction of applied longitudinal strains and j the direction of induced transverse strains [17]. To study the orientation dependence of PR, we first calculate C_{ij} in a CCS (X, Y, Z) where X is parallel to the lattice vector **a** and Z is parallel to **c**, as shown in Figs. 1(a)–1(c), then transform C_{ij} into a CCS (x, y, z) which is related to (X, Y, Z) by a rotation matrix $\widetilde{\boldsymbol{R}}$, and determine PR by $\nu_{ij} = -s_{ij}/s_{ii}$ in (x, y, z) with the rotated compliance tensor s_{ij} calculated from the transformed C_{ij} [55]. By successively rotating $\widetilde{\boldsymbol{R}}$ via its three Euler angles, we obtain the orientation-dependent PR and its global minimum $\nu_{\min}$ for each 3DGN in the 3D space. The strained direction of the global minimum $\nu_{\min}$ (referred to as the **P** direction hereinafter) and lattice vector **c** are used to define a reference CCS (x_0, y_0, z_0), as shown in Figs. 1(d) and 1(e), where x_0 is perpendicular to both the ***P*** direction and the **c** axis, and z_0 is parallel to the **c** axis. The angles between the lattice vector **a** and the x_0 axis, **b** and y_0, and **c** and the ***P*** direction obtained are (36.9°, 55.6°, 12°) for A33, (0°, 0°, 20°) for Z33, and (45°, 45°, 25°) for T44.

III. RESULTS AND DISCUSSIONS

A. Giant negative Poisson ratio near equilibrium structures

In Figs. 1(f) and 1(g), we plot parts of the calculated PRs of the 3DGNs where the maximum $\nu_{z,\max}$ and minimum $\nu_{z,\min}$ PRs of the 3DGNs are plotted for longitudinal strains applied along the z axes rotated relative to the strained direction ***P*** along which leads to the global minimum PR [see Figs. 1(d) and 1(e)]. The calculated global minimum PR ($\nu_{\min}$), the minimum PR ($\nu_{c,\min}$) when strained along their **c** axes, bulk

TABLE II. The calculated global minimum PR $\nu_{\min}$, minimum PR under strains along the direction of the **c** axis, $\nu_{c,\min}$, bulk modulus K (in GPa), shear modulus G (in GPa), Young's modulus Y (in GPa), total-energy difference relative to that of graphite, ΔE (in eV/atom), and universal anisotropy index A^U of the 3DGNs.

3DGN	ν_{min}	$\nu_{c,\min}$	K	G	Y	ΔE	A^U
A33	−8.50	−1.00	86	58	142	0.207	219.5
Z33	−2.60	−0.16	160	80	196	0.135	38.8
T44	−1.34	0.09	266	131	322	0.330	17.7

modulus K, shear modulus G, Young's modulus Y evaluated by the Voigt-Reuss-Hill (VRH) average [56], and the total-energy difference relative to that of graphene, ΔE of the 3DGNs, are listed in Table II. It is intriguing that all these 3DGNs possess strong NPR behavior, with $\nu_{\min}$ ranging from −1.34 to −8.50. The NPR up to −8.50 is a very negative NPR value compared with all the reported inorganic auxetic crystals [9] so far (see Tables S2 and S3 and detailed discussion in the SM [41]). The calculated energy difference ΔE is close to the previous results [31,39,40] with small deviations coming from the fact that the van der Waals interactions are considered in our calculation by the DFT-D2 method [53] which were neglected previously. The results of ΔE show that, thermodynamically, Z33 is relatively more (meta-) stable, followed by A33 and T44.

The 3DGNs are structurally anisotropic, due to their one-dimensional capillary pore structures, resulting in much larger elastic constant C_{33} components compared with C_{11} and C_{22} (see Table I). The universal anisotropy indexes $A^U = 5G_V/G_R + K_V/K_R - 6$ proposed by Ranganathan and Ostoja-Starzewski [57] are also listed in Table II to quantify the elastic anisotropy of these 3DGNs, where K_V, K_R, G_V, G_R are the bulk and shear modulus calculated by the Voigt and Reuss average methods. It has been demonstrated and is applicable to all types of single crystals that A^U is closely correlated with the auxetic behavior of a material [21,57], as shown in Table II. When strained along the **c** axis, the minimum PR values $\nu_{c,\min}$ reach −1.00 and −0.16 for the A33 and Z33 structures, respectively, while for the T44 structure, no NPR behavior is observed in any transverse direction due to the high symmetry of its **a**-**b** plane. As will be shown below, however, by applying biaxial stresses to introduce additional anisotropy, we can effectively manipulate and enhance their (axial) NPRs. The calculated bulk and shear moduli all exceed 55 GPa, indicating that these 3DGNs are mechanically strong, which is important for their applications in designing mechanical and electronic devices.

The structures investigated in the present work are part of a larger family of carbon allotropes [31,39,40]. Additional calculations of the elastic constants C_{ij} for the 3DGN structures with possible longer or shorter links were performed. The calculated global minimum Poisson ratios $\nu_{\min}$, minimum eigenvalues $\lambda_{\min}$ of the elastic matrix C_{ij}, and universal anisotropy indexes A^U for different structures are listed in Table S4 in the SM [41]. The results show that, on the one hand, increasing link lengths result in an increase in the NPR due to a higher structural anisotropy characterized by a larger pore cross-sectional area and a lower mass density. On the other hand, increasing link lengths can lead to a fast decrease in the mechanical stability of the structures, which is verified by the reduced minimum eigenvalues $\lambda_{\min}$ of the elastic matrix C_{ij} in our calculations given in Table S4 in the SM [41], consistent with the increased linear compressibility, decreased shear modulus and phonon-softening behavior in the previous first-principles calculations [31,39,40]. The structural instability and transformation in Ann and Tnn as their link lengths increase from A33 to A44 or T44 to T88 are clearly shown in Fig. S2 in the SM [41], where the initial and fully relaxed structures of A44, Z44, and T88 are plotted. The interlayer distance in the relaxed A44 and T88 structures is close to that in the graphite. However, by comparing the minimum eigenvalues $\lambda_{\min}$ of the elastic matrix C_{ij} for Z44 (2.65) and A33 (0.66), we expect that the stable Znn structures can have longer links and stronger NPRs.

B. Colossal auxetic expansions and contractions under large strains

The mechanical and NPR properties discussed above are based on the equilibrium structures and elastic theory. However, for applications as mechanical materials, such as sport protective equipment and crash energy absorption parts [4,8], the 3DGNs need to sustain large strains and experience plastic deformations [58–60]. Therefore, we apply large longitudinal strains $\epsilon_{P,L}$ to the 3DGNs in the $\boldsymbol{P}$ direction [see Figs. 1(d) and 1(e)], which leads to $\nu_{\min}$. The calculated longitudinal stresses $\sigma_{P,L}$ are presented in Figs. 2(a)–2(c), where the vertical arrows indicate the critical strains before structural instabilities either by reaching the peak stresses (mechanical instability) under tensile strains or experiencing phonon softening (dynamical instability) under compressive strains [61] (see Fig. S3 in the SM [41]). All 3DGNs can sustain large tensile stresses above 50 GPa under stretching ($\epsilon_{P,L} > 0$), higher than the ideal tensile strength of superhard cubic boron nitride [62]. However, under compression ($\epsilon_{P,L} < 0$), phonon instabilities occur early at small strains for A33, while Z33 and T44 display a much larger ductility, with compressive strengths higher than 10 GPa, larger than the ideal compressive strength of many metals [63,64]. Figures 2(a)–2(c) also plot the calculated strain relations $\epsilon_{P,T} - \epsilon_{P,L}$, with the transverse strain $\epsilon_{P,T}$ describing the maximum auxetic lateral expansion (or contraction). The nonlinearities of the $\epsilon_{P,T} - \epsilon_{P,L}$ curves indicate that their auxetic behavior depends on both the directions (the $\boldsymbol{P}$ direction) and magnitudes of the applied strains.

Figures 2(d)–2(f) plot the calculated (true) PRs at finite strains, defined as $\nu = -d\epsilon_{P,T}/d\epsilon_{P,L}$ [13], from the strain relations in Figs. 2(a)–2(c) fit piece-wise by cubic polynomials. At the equilibrium, the corresponding NPRs are −8.67, −2.55, and −1.32 for A33, Z33, and T44, respectively, very close to the minimum NPR values obtained by the elastic theory in Table II. It is interesting to note that the NPRs all decrease quickly under compression, showing strong compressive auxetic effects. For instance, the NPR of Z33 decreases from −2.6 at $\epsilon_{P,L} = 0$ to −6.2 at $\epsilon_{P,L} = -0.09$ before phonon instability sets in. For many auxetic crystals, such as cubic metals [5], their NPR effect in one direction in the cross-section plane vertical to the longitudinal strains are more than

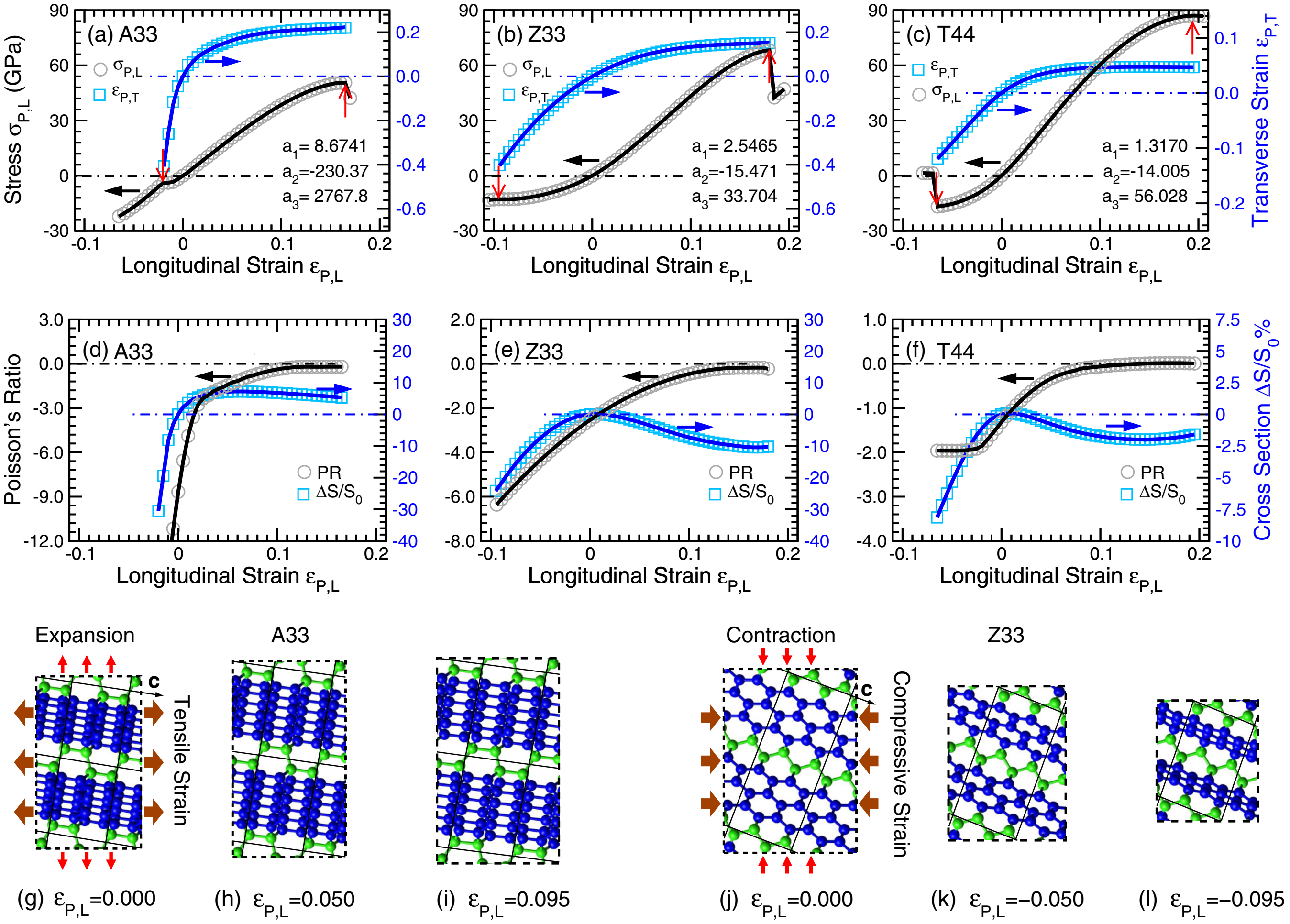

FIG. 2. (a)–(c) Longitudinal stresses $\sigma_{P,L}$ and maximum auxetic transverse strains $\epsilon_{P,T}$ for A33, Z33, and T44 under longitudinal strains $\epsilon_{P,L}$ applied in the ***P*** direction. Vertical arrows indicate the critical strains of structural instability set either by the peak stresses under tensile ($\epsilon_{P,L} > 0$) or soft phonons under compressive strains ($\epsilon_{P,L} < 0$). The smooth $\epsilon_{P,T}$-$\epsilon_{P,L}$ (blue) curves are fit by cubic polynomials with the fitting parameters listed in the figure. (d)–(f) PRs ($\nu = -d\epsilon_{P,T}/d\epsilon_{P,L}$) and cross-sectional area variations, $(S - S_0)/S_0$, relative to that at equilibrium S_0 and vertical to longitudinal strains applied in the ***P*** direction, for A33, Z33, and T44. (g)–(l) Structure snapshots of A33 and Z33 at different tensile and compressive strains applied in the ***P*** direction. Dashed-line boxes indicate the real scaled lateral expansion and contraction of the structures under tensile and compressive strains, respectively.

compensated by an even larger positive PR (PPR) effect in another normal direction, resulting in a regular behavior for the cross-sectional area; that is, the cross-sectional area decreases (or increases) under longitudinal tensile (or compressive) strains. There exists, however, exceptional cases, such as α quartz [65], where the average PRs on some crystalline planes are negative. Figures 2(d)–2(f) also plot the calculated variation of the cross-sectional area, $(S - S_0)/S_0$, relative to that at equilibrium S_0 and vertical to longitudinal strains in the ***P*** direction. It is obvious that the cross-sectional areas of all the 3DGNs decrease under compression, showing exceptional NPR effects similar to that in α quartz [65]. Under stretching, however, the cross-sectional areas of Z33 and T44 decrease, like regular materials, while for A33 its cross-sectional area enlarges quickly at the beginning and then reduces slightly under large tensile strains.

Figures 2(g)–2(l) show the calculated structure snapshots of A33 and Z33 under tensile and compressive strains in the ***P*** direction, respectively. A33 demonstrates the largest transverse expansion (22%) under tensile strains, followed by that (15%) of Z33. While under compression, both A33 and Z33 exhibit strong transverse contractions (40%), with Z33 displaying a much larger compressive ductility [see Figs. 2(a) and 2(b)]. Such a colossal auxetic transverse contraction of 40% (or expansion of 15%–22%) under compressive (or tensile) strains is striking when compared with the available results in the literatures for both 3D and 2D materials [11–14,37] and makes the 3DGNs an excellent NPR material for applications under large strains [58–60].

C. Mechanism for giant negative Poisson ratio in three-dimensional graphene networks

To better understand the underlying mechanism leading to the giant NPRs and transverse expansions or contractions in the 3DGNs, we analyze in Figs. 3(a) and 3(b) the variations in local atomic bond angles and bond lengths during the compressive strain loading process with Z33 as a

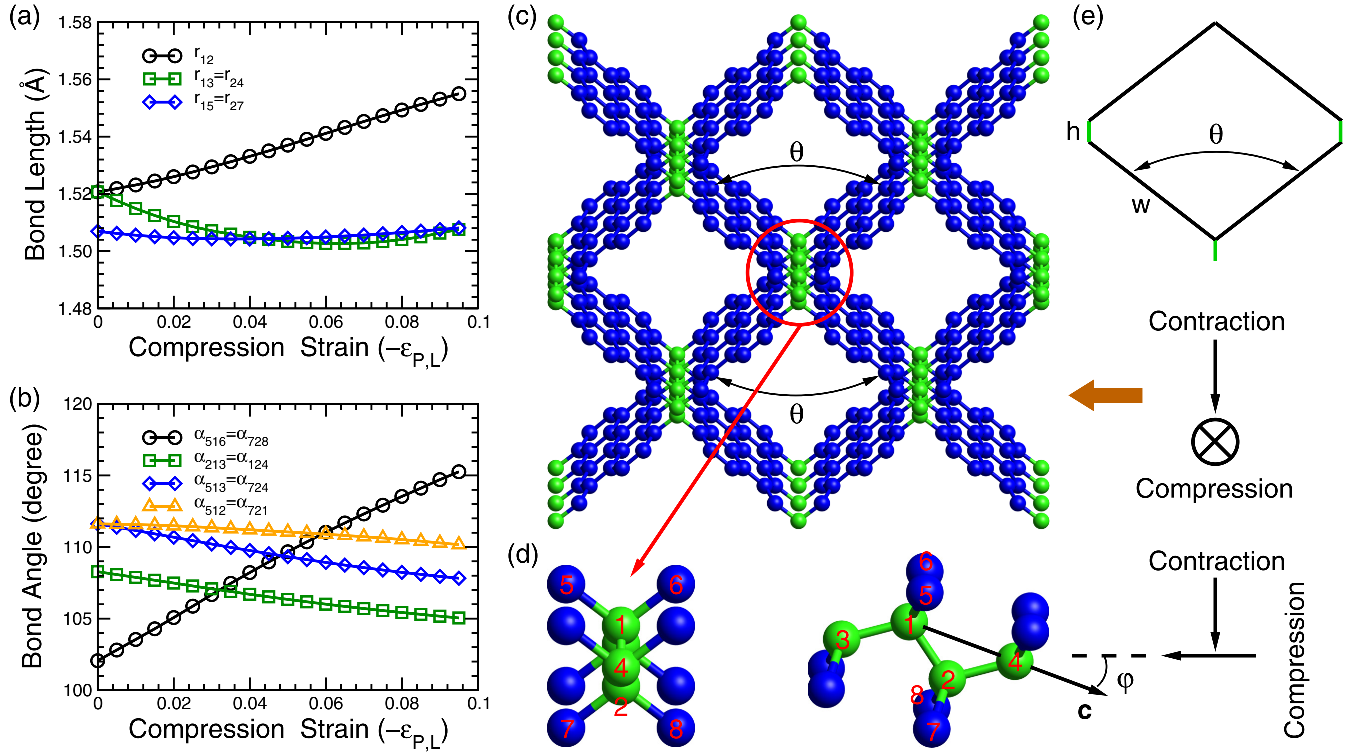

FIG. 3. The calculated variations of (a) the local bond lengths and (b) bond angles at one link junction between two carbon ribbons in Z33 under compression in the ***P*** direction, with the bond lengths and bond angles defined in panel (d). (c) The cross section of the Z33 supercell with the compression vertically pointing into the cross section. A side view of the Z33 supercell is given in Figs. 2(j)–2(l). (d) The front and side views of a local sp^3 carbon bonding at the link junction where the bond angle $\alpha_{516} = \alpha_{728}$ mainly determines the dihedral angle θ between two carbon ribbons in Z33. (e) A sketch of the cross-sectional area of Z33 normal to the **c** axis, defining the width w of the carbon ribbon, the height h of the link junction layer, and the angle φ between the **c** axis and direction of the applied compression.

typical example. Under the compression, the bond lengths do not change much (within 2.5%), while the bond angle α_{516} ($=\alpha_{728}$) which determines the dihedral angle θ [see Figs. 3(c) and 3(d)] between two carbon ribbons increase quickly. The monotonic and quick increase in θ leads to the continuous and large contraction of Z33 along the diagonal direction and results in the giant NPR. The cross-sectional area per supercell vertical to the compression direction is proportional to $S = [w^2\sin\theta + 2hw\sin(\theta/2)]\cos\varphi$, as indicated in Fig. 3(e). If we neglect the variation in the width w of the carbon ribbon, height h of the link junction layer, and angle φ between the **c** axis and applied strain direction during the compression, we obtain approximately the variation of S relative to that at equilibrium S_0, $\Delta S/S_0 = \sin(\theta/2)[\cos(\theta/2) + h/w]/\{\sin(\theta_0/2)[\cos(\theta_0/2) + h/w]\} - 1$, which decreases as θ ($102^\circ < \theta < 115^\circ$) further increases under the compression. Using the calculated results in Fig. 3(b), where $\theta_0 = 102^\circ$, $h/w = 0.1116$ at equilibrium, and the maximum $\theta = 115^\circ$, we have the maximum reduction $\Delta S/S_0 = -0.05$. Comparing with the accurate result, $\Delta S/S_0 = -0.24$ [see Fig. 2(e)], the simple estimation produces the correct trend but drastically underestimates the NPR effect, indicating distinct variations in w, h, and φ during compression. The increase in θ under compression intensifies the anisotropy in the cross section of Z33, as shown in Fig. 3(e), which enhances the NPR behavior of Z33 under compression, as plotted in Figs. 2(b) and 2(e). Although the detailed processes are slightly different, we find that the sp^3 bonding at the link junctions of the 3DGNs all work as transformers turning the applied strains into anisotropic bond angle distortions which give rise to the auxetic behavior in these structures. To the best of our knowledge, such NPR underlying mechanism has not been reported previously.

The orientation-dependent NPR results we obtained in Fig. 1(f) can be discussed from the in-plane anisotropy point of view. Figure 4 plots sketches of a $1 \times 1 \times n$ supercell for any 3DGN under longitudinal strains applied in different directions as those in Fig. 1(d). When strained along the **c** axis [Fig. 4(a)], the symmetry of the cross section vertical to the applied strain varies from highly anisotropic (A33), to slightly anisotropic (Z33), and to perfectly symmetric (T44), as shown in Figs. 1(a)–1(c). NPRs reaching -1.00 and -0.16 are found in A33 and Z33, respectively, due to the strain induced sp^3 bond angle anisotropic distortions at the link junctions, similar to that discussed in Fig. 3, while only the PPR effect was observed in T44 [see Fig. 1(f) and Table II]. When the strain is applied vertically to the **c** axis [Fig. 4(b)], the lateral structure variation along the **c** axis becomes practically zero due to the strong tensile strength of the carbon ribbons, and NPRs approach zero for all the 3DGNs [see Fig. 1(f)]. In between these two extreme cases, there exists a specific ***P*** direction of applied strains where NPR reaches its minimum. The cross

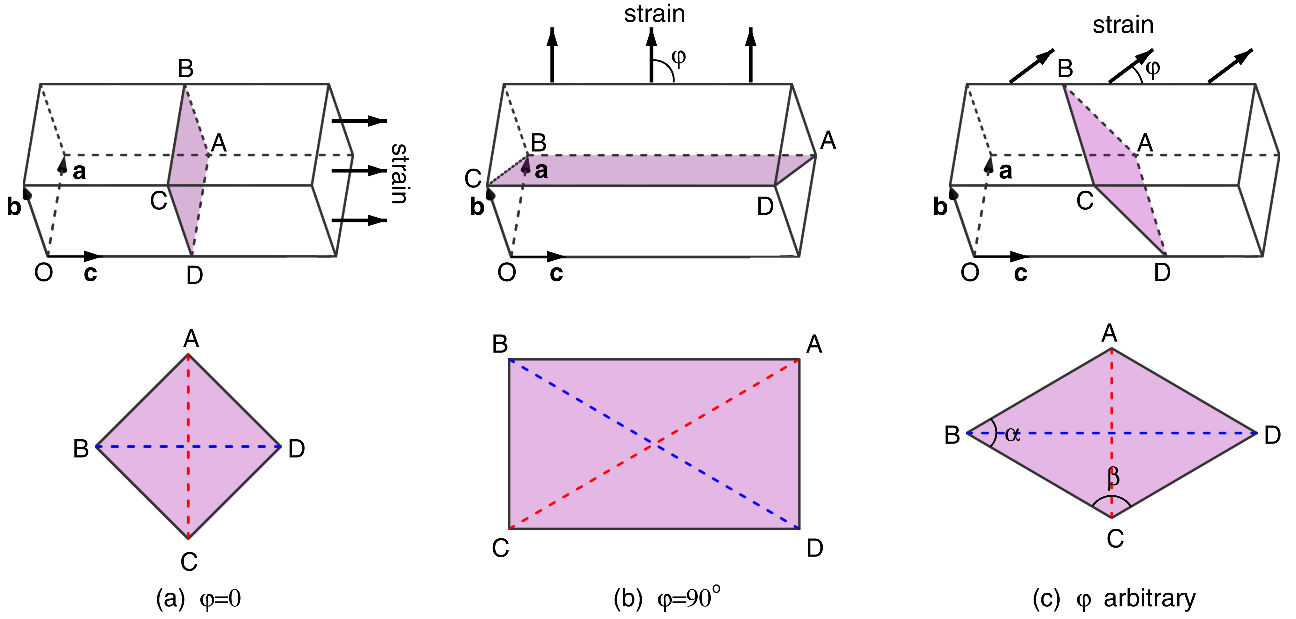

FIG. 4. The sketches of a 1 × 1 × *n* supercell for any 3DGN under (tensile or compressive) strains in different directions corresponding to those in Fig. 1(d), with the cross-sectional area vertical to the directions of applied strains (a) normal to, (b) parallel to, and (c) at an arbitrary angle with the **c** axis.

section vertical to the direction of the strains applied at an angle to the **c** axis [Fig. 4(c)] becomes anisotropic for all the 3DGNs, which facilitates the bond angle distortions at the link junctions of carbon ribbons as the applied strains increase and gives rise to giant NPRs, as shown in Fig. 1(f) and Table II.

It it worth noting that, for isotropic materials even though the PRs are predicted to vary between -1 and 0.5 [4], they appear uniformly in all directions. For example, NPR down to -0.7 has been achieved in isotropic foams [4], and rubber honeycomb structures displaying a NPR close to -1 isotropically in the 2D plane were observed [66]. The auxetic effects in these materials are also strong. Therefore, anisotropy is not an indispensable prerequisite for a strong NPR. However, for auxetic materials with NPRs (< -1) out of the range $-1 < \nu_{\min} < 0$ along specific directions as we investigated in the present work, anisotropy plays a crucial role.

D. Manipulation of negative Poisson ratios with biaxial stresses

The above analysis allows one to effectively manipulate the NPRs by biaxial stresses that increase the in-plane anisotropy in the cross sections of the 3DGNs vertical to the applied strains. As an illustration, Fig. 5 shows the emerging NPR behavior of T44 when strained along the **c** axis with a constant biaxial stress applied simultaneously in the *y* direction (see Computational details). The highly symmetrical cross section of T44 normal to the **c** axis shows a small PPR (<0.1) when uniaxial strains are exerted along the **c** axis [black dash-dotted curves in Figs. 5(a) and 5(b)]. By applying a biaxial compressive ($\sigma_{yy} = -3$ GPa) or tensile ($\sigma_{yy} = 5$ GPa) stress in the *y* direction, however, the PR of T44 turns negative with $\nu_{zy} = -d\epsilon_{yy}/d\epsilon_{zz} = -0.43$ (for $\sigma_{yy} = -3$ GPa) or $\nu_{zx} = -d\epsilon_{xx}/d\epsilon_{zz} = -0.25$ (for $\sigma_{yy} = 5$ GPa) at $\epsilon_{zz} = 0$, respectively, which are further enhanced to -2.6 and -1.2 under large compressive strains ($\epsilon_{zz} \rightarrow -0.04$) [black solid and dashed curves in Fig. 5(a) and 5(b)]. Furthermore, the cross-sectional area of T44 decreases under compressive strains ($\epsilon_{zz} < 0$) applied along the **c** axis, indicating a dominant NPR effect, as revealed by the blue solid and dashed curves in Fig. 5(a). The manipulation of NPRs in T44 can be explained by the variation of the dihedral angle θ between two carbon nanoribbons defined in Figs. 5(c) and 5(d). Without biaxial stresses, θ does not change under applied strains in the **c** axis, due to the high symmetry in the cross section [see Fig. 1(c)]. A biaxial compressive (or tensile) stress σ_{yy} lowers the symmetry of the cross section by decreasing (or increasing) θ_0 at equilibrium, and the applied compressive strains ($\epsilon_{zz} < 0$) induce further decrease (or increase) in θ [see Fig. 5(e)], leading to a strong and sensitive NPR contraction in ϵ_{yy} (or ϵ_{xx}).

In our calculations, we apply a biaxial compressive ($\sigma_{yy} = -3$ GPa) or tensile ($\sigma_{yy} = 5$ GPa) stress in the *y* direction, so it generates about the same degrees of anisotropy in the cross section of T44 normal to the strains applied along its **c** or *z* axis, which induces auxetic strains in ϵ_{yy} (for $\sigma_{yy} = -3$ GPa) or in ϵ_{xx} (for $\sigma_{yy} = 5$ GPa), as shown in Figs. 5(c) and 5(d). The results indicate that biaxial compressive stresses are more effective in manipulating NPRs in the 3DGNs. The NPR mechanism in T44 is similar to that of Z33, as we discussed in Fig. 3, where the sp^3 bonds at the link junctions of the carbon ribbons turn the applied strains into anisotropic bond angle distortions giving rise to the auxetic behavior in T44, when its cross section normal to the applied strains becomes anisotropic under biaxial stresses (σ_{yy}). We expect that such manipulation and enhancement of NPR behavior by multiaxial stress settings can be achieved in many auxetic and normal materials, opening a new direction to search and design strong auxetic materials.

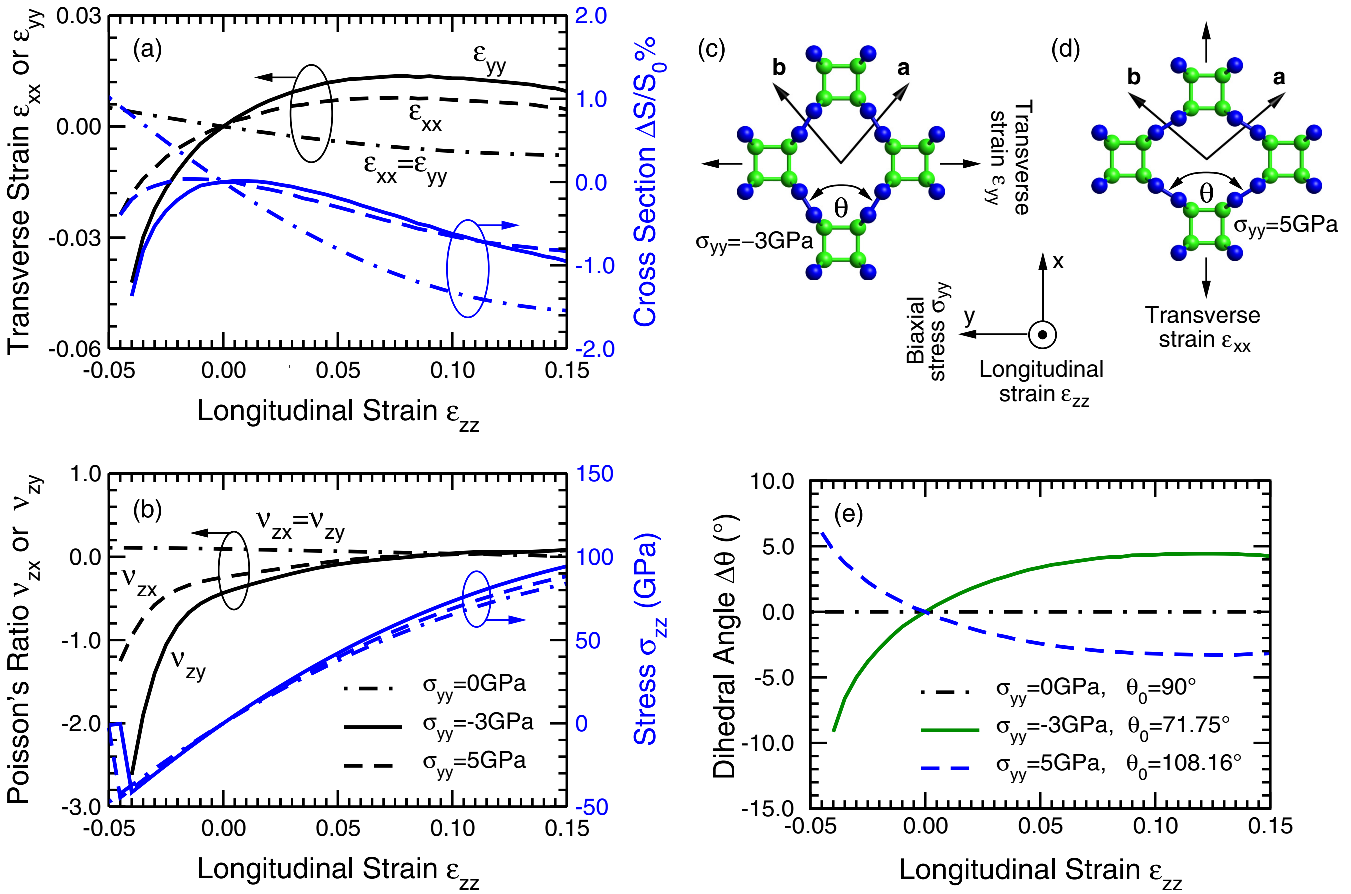

FIG. 5. (a) The calculated transverse strain ϵ_T (ϵ_{xx} or ϵ_{yy}) and cross-sectional area variation, $\Delta S/S_0$, relative to that at equilibrium S_0, and (b) the corresponding PR ($-d\epsilon_T/d\epsilon_{zz}$) and longitudinal stress σ_{zz}, for T44 induced by longitudinal strains (ϵ_{zz}) along its **c** axis when a constant biaxial compressive ($\sigma_{yy} < 0$) or tensile ($\sigma_{yy} > 0$) stress is applied. (c), (d) The equilibrium cross-sectional structure of T44 normal to its **c** axis under a constant biaxial compressive ($\sigma_{yy} = -3$ GPa) and tensile ($\sigma_{yy} = 5$ GPa) stress applied in the y direction. (e) The variations of the dihedral angle $\Delta\theta = \theta - \theta_0$ between two carbon ribbons in T44 under longitudinal strains applied in the **c** axis direction, with different biaxial stresses (σ_{yy}).

IV. CONCLUSIONS

NPR behavior of three typical IGN-type 3DGNs, composed of sp^2 graphene nanoribbons and sp^3 carbon link junctions, is predicted by first-principles calculations both at equilibrium and under large uniaxial loading strains. All the 3DGNs show strong auxetic behavior, with the minimum NPRs up to -8.50 and colossal transverse contractions (expansions) of over 40% (20%), when compressed (stretched) along specific directions. By anisotropy arguments and careful analyses of the deformation patterns of the local atomic bonding configurations at the link junctions during the straining processes, a mechanism dominated by sp^3 carbon bond angle distortion and cross-section in-plane anisotropy variation is revealed, which is expected to apply to many 3DGNs and similar structures. It is further demonstrated that by applying biaxial stresses to increase in-plane anisotropy, one can effectively manipulate and enhance the NPRs in these 3DGNs, providing a way for rational design and utilization of NPR materials. These discoveries add another extraordinary mechanical characteristic to many of their unique physical and chemical properties in the 3DGNs, which will broaden the practical applications of the 3DGNs as multifunctional materials.

ACKNOWLEDGMENTS

This work was supported by the National Natural Science Foundation of China (Grant No. 11974237) and Ministry of Science and Technology of China (Grant No. 2016-YFA0300500). Computations were performed at the Center for High Performance Computing, Shanghai Jiao Tong University.

---

[1] K. E. Evans, M. A. Nkansah, I. J. Hutchinson, and S. C. Rogers, Molecular network design, Nature (London) **353**, 124 (1991).

[2] R. H. Baughman, S. Stafström, C. Cui, and S. O. Dantas, Materials with negative compressibilities in one or more dimensions, Science **279**, 1522 (1998).

[3] T. A. Mary, J. S. O. Evans, T. Vogt, and A. W. Sleight, Negative thermal expansion from 0.3 to 1050 kelvin in ZrW_2O_8, Science **272**, 90 (1996).

[4] R. Lakes, Foam structures with a negative Poisson's ratio, Science **235**, 1038 (1987).

[5] R. H. Baughman, J. M. Shacklette, A. A. Zakhidov, and S. Stafström, Negative Poisson's ratios as a common feature of cubic metals, Nature (London) **392**, 362 (1998).

[6] O. Sigmund, S. Torquato, and I. A. Aksay, On the design of 1–3 piezocomposites using topology optimization, J. Mater. Res. **13**, 1038 (1998).

[7] F. Scarpa, Auxetic materials for bioprostheses, IEEE Signal Process. Mag. **25**, 128 (2008).

[8] F. Scarpa, L. G. Ciffo, and J. R. Yates, Dynamic properties of high structural integrity auxetic open cell foam, Smart Mater. Struct. **13**, 49 (2003).

[9] S. Chibani and F.-X. Coudert, Systematic exploration of the mechanical properties of 13621 inorganic compounds, Chem. Sci. **10**, 8589 (2019).

[10] M. Bowick, A. Cacciuto, G. Thorleifsson, and A. Travesset, Universal Negative Poisson Ratio of Self-Avoiding Fixed-Connectivity Membranes, Phys. Rev. Lett. **87**, 148103 (2001).

[11] J. Jiang and H. S. Park, Negative Poisson's ratio in single-layer black phosphorus, Nat. Commun. **5**, 4727 (2014).

[12] J. N. Grima, S. Winczewski, L. Mizzi, M. C. Grech, R. Cauchi, R. Gatt, D. Attard, K. W. Wojciechowski, and J. Rybicki, Tailoring graphene to achieve negative Poisson's ratio properties, Adv. Mater. **27**, 1455 (2015).

[13] L. Yu, Q. Yan, and A. Ruzsinszky, Negative Poisson's ratio in 1T-type crystalline two-dimensional transition metal dichalcogenides, Nat. Commun. **8**, 15224 (2017).

[14] Y. Du, J. Maassen, W. Wu, Z. Luo, X. Xu, and P. D. Ye, Auxetic black phosphorus: A 2D material with negative Poisson's ratio, Nano Lett. **16**, 6701 (2016).

[15] D. T. Ho, S.-D. Park, S.-Y. Kwon, K. Park, and S. Y. Kim, Negative Poisson's ratios in metal nanoplates, Nat. Commun. **5**, 3255 (2014).

[16] D. T. Ho, S.-Y. Kwon, and S. Y. Kim, Metal [100] nanowires with negative Poisson's ratio, Sci. Rep. **6**, 27560 (2016).

[17] A. Alderson and K. E. Evans, Molecular Origin of Auxetic Behavior in Tetrahedral Framework Silicates, Phys. Rev. Lett. **89**, 225503 (2002).

[18] Y. Suzuki, G. Cardone, D. Restrepo, P. D. Zavattieri, T. S. Baker, and F. A. Tezcan, Self-assembly of coherently dynamic, auxetic, two-dimensional protein crystals, Nature (London) **533**, 369 (2016).

[19] J. I. Lipton, R. MacCurdy, Z. Manchester, L. Chin, D. Cellucci, and D. Rus, Handedness in shearing auxetics creates rigid and compliant structures, Science **360**, 632 (2018).

[20] G. P. T. Choi, L. H. Dudte, and L. Mahadevan, Programming shape using kirigami tessellations, Nat. Mater. **18**, 999 (2019).

[21] Z. A. D. Lethbridge, R. I. Walton, A. S. H. Marmier, C. W. Smith, and K. E. Evans, Elastic anisotropy and extreme Poisson's ratios in single crystals, Acta Mater. **58**, 6444 (2010).

[22] A. U. Ortiz, A. Boutin, A. H. Fuchs, and F.-X. Coudert, Anisotropic Elastic Properties of Flexible Metal-Organic Frameworks: How Soft are Soft Porous Crystals? Phys. Rev. Lett. **109**, 195502 (2012).

[23] R. H. Baughman and D. S. Galvão, Crystalline networks with unusual predicted mechanical and thermal properties, Nature (London) **365**, 735 (1993).

[24] X. Wang, Y. Zhang, C. Zhi, X. Wang, D. Tang, Y. Xu, Q. Weng, X. Jiang, M. Mitome, D. Golberg, and Y. Bando, Three-dimensional strutted graphene grown by substrate-free sugar blowing for high-power-density supercapacitors, Nat. Commun. **4**, 2905 (2013).

[25] Y. Zhang, Y. Huang, T. Zhang, H. Chang, P. Xiao, H. Chen, Z. Huang, and Y. Chen, Broadband and tunable high-performance microwave absorption of an ultralight and highly compressible graphene foam, Adv. Mater. **27**, 2049 (2015).

[26] Q. Zhang, X. Xu, D. Lin, W. Chen, G. Xiong, Y. Yu, T. S. Fisher, and H. Li, Hyperbolically patterned 3D graphene metamaterial with negative Poisson's ratio and superelasticity, Adv. Mater. **28**, 2229 (2016).

[27] Z. Huang, H. Chen, Y. Huang, Z. Ge, Y. Zhou, Y. Yang, P. Xiao, J. Liang, T. Zhang, Q. Shi, G. Li, and Y. Chen, Ultra-broadband wide-angle terahertz absorption properties of 3D graphene foam, Adv. Funct. Mater. **28**, 1704363 (2018).

[28] K. Zhao, T. Zhang, H. Chang, Y. Yang, P. Xiao, H. Zhang, C. Li, C. S. Tiwary, P. M. Ajayan, and Y. Chen, Super-elasticity of three-dimensionally cross-linked graphene materials all the way to deep cryogenic temperatures, Sci. Adv. **5**, eaav2589 (2019).

[29] N. V. Krainyukova and E. N. Zubarev, Carbon Honeycomb High Capacity Storage for Gaseous and Liquid Species, Phys. Rev. Lett. **116**, 055501 (2016).

[30] M. Hu, J. He, Z. Zhao, T. A. Strobel, W. Hu, D. Yu, H. Sun, L. Liu, Z. Li, M. Ma, Y. Kono, J. Shu, H. Mao, Y. Fei, G. Shen, Y. Wang, S. J. Juhl, J. Y. Huang, Z. Liu, B. Xu, and Y. Tian, Compressed glassy carbon: An ultrastrong and elastic interpenetrating graphene network, Sci. Adv. **3**, e1603213 (2017).

[31] Y. Lin, Z. Zhao, T. A. Strobel, and R. E. Cohen, Interpenetrating graphene networks: Three-dimensional node-line semimetals with massive negative linear compressibilities, Phys. Rev. B **94**, 245422 (2016).

[32] Z. Pang, X. Gu, Y. Wei, R. Yang, and M. S. Dresselhaus, Bottom-up design of three-dimensional carbon-honeycomb with superb specific strength and high thermal conductivity, Nano Lett. **17**, 179 (2017).

[33] J. Liu, T. Zhao, S. Zhang, and Q. Wang, A new metallic carbon allotrope with high stability and potential for lithium ion battery anode material, Nano Energy **38**, 263 (2017).

[34] J. Hu, W. Wu, C. Zhong, N. Liu, C. Ouyang, H. Y. Yang, and S. A. Yang, Three-dimensional honeycomb carbon: Junction line distortion and novel emergent fermions, Carbon **141**, 417 (2019).

[35] Y. Chen, Y. Xie, X. Yan, M. L. Cohen, and S. Zhang, Topological carbon materials: A new perspective, Phys. Rep. **868**, 1 (2020).

[36] J.-T. Wang, S. Nie, H. Weng, Y. Kawazoe, and C. Chen, Topological Nodal-Net Semimetal in A Graphene Network Structure, Phys. Rev. Lett. **120**, 026402 (2018).

[37] J. Zhang and Q. Xiong, The negative Poisson's ratio in graphene-based carbon foams, Phys. Chem. Chem. Phys. **20**, 4597 (2018).

[38] W. Wang, C. He, L. Xie, and Q. Peng, The temperature-sensitive anisotropic negative Poisson's ratio of carbon honeycomb, Nanomaterials **9**, 487 (2019).

[39] Z. Zhao, B. Xu, L.-M. Wang, X.-F. Zhou, J. He, Z. Liu, H.-T. Wang, and Y. Tian, Three dimensional carbon-nanotube polymers, ACS Nano **5**, 7226 (2011).

[40] X. Jiang, J. Zhao, Y.-L. Li, and R. Ahuja, Tunable assembly of sp^3 cross-linked 3D graphene monoliths: A first-principles prediction, Adv. Funct. Mater. **23**, 5846 (2013).

[41] See Supplemental Material at http://link.aps.org/supplemental/10.1103/PhysRevB.102.184116 for more information on the 3D atomic structures and atomic positions of the 3DGNs, discussion of the minimum Poisson's ratio in inorganic compounds, NPRs and mechanical stabilities of 3DGNs with different link lengths, and the phonon spectra of the 3DGNs.

[42] F. Mouhat and F.-X. Coudert, Necessary and sufficient elastic stability conditions in various crystal systems, Phys. Rev. B **90**, 224104 (2014).

[43] G. Kresse and J. Furthmüller, Efficient iterative schemes for *ab initio* total-energy calculations using a plane-wave basis set, Phys. Rev. B **54**, 11169 (1996).

[44] G. Kresse and D. Joubert, From ultrasoft pseudopotentials to the projector augmented-wave method, Phys. Rev. B **59**, 1758 (1999).

[45] J. P. Perdew, K. Burke, and M. Ernzerhof, Generalized Gradient Approximation Made Simple, Phys. Rev. Lett. **77**, 3865 (1996).

[46] H. J. Monkhorst and J. D. Pack, Special points for Brillouin-zone integrations, Phys. Rev. B **13**, 5188 (1976).

[47] Z. Pan, H. Sun, Y. Zhang, and C. Chen, Harder than Diamond: Superior Indentation Strength of Wurtzite BN and Lonsdaleite, Phys. Rev. Lett. **102**, 055503 (2009).

[48] B. Li, H. Sun, and C. Chen, Large indentation strain-stiffening in nanotwinned cubic boron nitride, Nat. Commun. **5**, 4965 (2014).

[49] D. Roundy, C. R. Krenn, M. L. Cohen, and J. W. Morris, Ideal Shear Strengths of fcc Aluminum and Copper, Phys. Rev. Lett. **82**, 2713 (1999).

[50] M. Takagi, T. Taketsugu, H. Kino, Y. Tateyama, K. Terakura, and S. Maeda, Global search for low-lying crystal structures using the artificial force induced reaction method: A case study on carbon, Phys. Rev. B **95**, 184110 (2017).

[51] L. Shi, A. Xu, and T. Zhao, Three-dimensional carbon-honeycomb as nanoporous lithium and sodium deposition scaffold, J. Phys. Chem. C **122**, 21262 (2018).

[52] X. Li, J. Liu, F. Q. Wang, Q. Wang, and P. Jena, Rational design of porous nodal-line semimetallic carbon for K-ion battery anode materials, J. Phys. Chem. Lett. **10**, 6360 (2019).

[53] S. Grimme, Semiempirical GGA-type density functional constructed with a long-range dispersion correction, J. Comput. Chem. **27**, 1787 (2006).

[54] A. Togo, F. Oba, and I. Tanaka, First-principles calculations of the ferroelastic transition between rutile-type and $CaCl_2$-type SiO_2 at high pressures, Phys. Rev. B **78**, 134106 (2008).

[55] J. Dagdelen, J. Montoya, M. de Jong, and K. Persson, Computational prediction of new auxetic materials, Nat. Commun. **8**, 323 (2017).

[56] R. Hill, The elastic behavior of a crystalline aggregate, Proc. Phys. Soc., London, Sect. A **65**, 349 (1952).

[57] S. I. Ranganathan and M. Ostoja-Starzewski, Universal Elastic Anisotropy Index, Phys. Rev. Lett. **101**, 055504 (2008).

[58] K. Bertoldi, P. M. Reis, S. Willshaw, and T. Mullin, Negative Poisson's ratio behavior induced by an elastic instability, Adv. Mater. **22**, 361 (2010).

[59] J.-H. Lee, J. P. Singer, and E. L. Thomas, Micro-/nanostructured mechanical metamaterials, Adv. Mater. **24**, 4782 (2012).

[60] A. Clausen, F. Wang, J. S. Jensen, O. Sigmund, and J. A. Lewis, Topology optimized architectures with programmable Poisson's ratio over large deformations, Adv. Mater. **27**, 5523 (2015).

[61] D. M. Clatterbuck, C. R. Krenn, M. L. Cohen, and J. W. Morris, Phonon Instabilities and the Ideal Strength of Aluminum, Phys. Rev. Lett. **91**, 135501 (2003).

[62] Y. Zhang, H. Sun, and C. Chen, Superhard Cubic BC_2N Compared to Diamond, Phys. Rev. Lett. **93**, 195504 (2004).

[63] M. Černý and J. Pokluda, The theoretical strength of fcc crystals under multiaxial loading, Comput. Mater. Sci. **50**, 2257 (2011).

[64] A. Breidi, S. G. Fries, and A. V. Ruban, Ideal compressive strength of fcc Co, Ni, and Ni-rich alloys along the $\langle 001 \rangle$ direction: A first-principles study, Phys. Rev. B **93**, 144106 (2016).

[65] E. Kittinger, J. Tichý, and E. Bertagnolli, Example of a Negative Effective Poisson's Ratio, Phys. Rev. Lett. **47**, 712 (1981).

[66] L. J. Gibson, M. F. Ashby, G. S. Schajer, and C. I. Robertson, The mechanics of two-dimensional cellular materials, Proc. R. Soc. London, Ser. A **382**, 25 (1982).